



ANNUAL REVIEWS **Further**

Click [here](#) for quick links to Annual Reviews content online, including:

- Other articles in this volume
- Top cited articles
- Top downloaded articles
- Our comprehensive search

Laboratory-Frame Photoelectron Angular Distributions in Anion Photodetachment: Insight into Electronic Structure and Intermolecular Interactions

Andrei Sanov

Department of Chemistry and Biochemistry, University of Arizona, Tucson, Arizona 85721-0041; email: sanov@u.arizona.edu

Annu. Rev. Phys. Chem. 2014. 65:341–63

First published online as a Review in Advance on January 9, 2014

The *Annual Review of Physical Chemistry* is online at physchem.annualreviews.org

This article's doi:
10.1146/annurev-physchem-040513-103656

Copyright © 2014 by Annual Reviews.
All rights reserved

Keywords

photoelectron imaging, negative ions, photoelectron spectroscopy, partial waves

Abstract

This article provides an overview of some recent advances in the modeling of photoelectron angular distributions in negative-ion photodetachment. Building on the past developments in threshold photodetachment spectroscopy that first tackled the scaling of the partial cross sections with energy, depending on the angular momentum quantum number ℓ , it examines the corresponding formulation of the central potential model and extends it to the more general case of hybrid molecular orbitals. Several conceptual approaches to understanding photoelectron angular distributions are discussed. In one approach, the angular distributions are examined based on the contributions of the symmetry-allowed s and p partial waves of the photodetached electron. In another related approach, the parent molecular orbitals are described based on their dominant s and p characters, whereas the continuum electron is described in terms of interference of the corresponding $\Delta\ell = \pm 1$ photodetachment channels.

PAD: photoelectron angular distribution

LF: laboratory frame

MF: molecular frame

MO: molecular orbital

1. INTRODUCTION

In recent years, photoelectron imaging has become the spectroscopic technique of choice to study the photoionization of neutral molecules (1) and photodetachment of negative ions (2). The popularity of the imaging approach (3–6), particularly in the velocity-mapping implementation (7), is attributed not only to the straightforward, visual nature of the results, but also to the insight provided by the simultaneous observation of the energy spectra and angular distributions.

The photoelectron angular distributions (PADs) resulting from one-photon detachment or ionization provide insight into the properties of the corresponding parent orbitals (8–11). Modeling the PADs is not a trivial pursuit, but direct computations that account for the complexity of the electronic structure, wave interference, relaxation effects, and orientation averaging have been successfully demonstrated (10, 12–15). Unfortunately, the extensive details of the calculations may complicate the understanding of the underlying physics of photoemission. This review describes some recent successes in tackling molecular-anion photodetachment at a conceptual level, focusing not so much on the computational details, but on the analytical description of the process. The goal is to describe the photodetachment by relying, as much as possible, on the key physical concepts and a pen and paper only.

Angle-resolved photoelectron spectroscopy, aimed at unraveling angle-resolved spectra or energy-dependent angular distributions, has been an active area of research for nearly a century (16). PAD measurements have been made and are being carried out in various, often overlapping contexts, including single- and multiphoton photoionization of neutral atoms and molecules; atomic, molecular, and cluster anion photodetachment; time-resolved measurements (17); strong-field versus weak-field measurements; laboratory-frame (LF) versus molecular-frame (MF) PADs (12); and the photodetachment/photoionization of prealigned or oriented ensembles. Most of these themes are not discussed here, and the reader is referred to the extensive literature covering these topics. In particular, the review by Reid (10) discussed PADs in various contexts relevant to different experimental scenarios, primarily applicable to the photoionization of neutral molecules.

This review focuses on the photodetachment of negative ions and takes advantage of the unique opportunities afforded by the small photon energies needed to photodetach an electron and the usually weak interaction of the departing electron with the remaining neutral molecule. In stark contrast to neutral-molecule ionization, photodetachment processes at small to moderate energies are dominated by partial waves with the smallest allowed values of the orbital angular momentum quantum number, ℓ . This allows for significant simplifications in the qualitative understanding of the process.

Such simplifications afford unique opportunities in the related realm of the characterization of molecular bonding structures that often involves defining the primary character of molecular orbitals (MOs). For example, hybrid orbitals have long been used to predict molecular geometries and reactivity. Such general approaches have indisputable theoretical and pedagogical value. Whereas many modern theoretical methods aim to provide increasingly accurate and detailed descriptions of the electronic structure, demanding ever increasing computing power, the ultimate goal of scientific exploration remains the conceptual understanding of the big picture, such as the character of chemical bonds.

The dominant bond character, typically expressed in terms of their s , p , d , etc., components, is directly related to the above simplified description of the photodetached electron in terms of the smallest- ℓ partial waves. This review describes some recent work that capitalizes on this opportunity by dealing primarily with the s and p (and sometimes d) components of the MOs and the resulting continuum waves.

Although most modern angle-resolved experiments are carried out using photoelectron imaging spectroscopy (11, 18–48), the imaging technique itself is not the focus of this review. In fact, among the dual information content of photoelectron imaging—the PADs and the photoelectron spectra—only the energy-dependent PADs are discussed.

In a one-photon process with linearly polarized light, the LF PAD is generally described by the equation

$$I(\theta) = a[1 + \beta P_2(\cos \theta)], \quad (1)$$

where θ is the angle between the photoelectron velocity vector and the light's electric field vector (typically set along the LF z direction), a is a normalization constant proportional to the total photodetachment cross section, and $P_2(\cos \theta) = (1/2)(3\cos^2\theta - 1)$ is the second-order Legendre polynomial. β in Equation 1 is the anisotropy parameter ranging from -1 for perpendicular transitions to $+2$ for parallel transitions (8). This parameter fully characterizes the PAD and provides a direct indication of the character of the photodetachment process.

One goal of this review is to refute the perception that the information content of LF PADs automatically becomes limited for larger molecules with complex electronic structure. Although it is true that orientation averaging takes a toll on the amount of information observable in the LF, compared to MF measurements (10, 12, 49), the relative ease of LF experiments opens the door for extensive and less constrained investigations of a broader range of systems. Furthermore, as molecules increase in size, the PADs do often become less anisotropic, but this trend in itself, if analyzed properly, reflects the increasing richness and complexity of the electronic structure. A typical case of anisotropy decrease due to increased complexity is photodetachment from sp^n hybrid orbitals. Whereas the PADs for s and p orbital photodetachment are parallel and typically perpendicular, respectively (50), the PAD for photodetachment from a mixed-character state can fall anywhere between the two extremes (51). The anisotropy parameter gravitating toward zero in this case may contain valuable information about the character of the hybrid orbital (52) and, for example, the corresponding degree of aromaticity of the molecule being studied (53–55).

At the conceptual foundation of this work is the mathematical idea of basis-set expansion. As applied to molecular-anion photodetachment, this idea is introduced in Section 2, which also outlines the fundamental differences between the photodetachment and neutral-molecule photoionization processes. Section 3 summarizes the application of these ideas in the form of partial-wave expansion of the photodetached electron. In Section 4, the central potential model applicable to the photodetachment from atomic or atomic-like anions is discussed, followed by the extension of the model to the case of s - p mixed-character molecular states in Section 5.

2. BASIS-SET EXPANSION APPLIED TO PHOTODETACHMENT

This review adopts the MO description of the electronic structure of molecules and considers the photodetachment in the Koopmans' theorem (56) spirit, neglecting configuration interaction, vibronic coupling, and relaxation effects. The electronic wave function of the anion is factored into the wave function of the neutral core and the MO being vacated. The final state is described similarly as the product of the remaining neutral and the free electron.

It is often convenient to expand the free-electron wave in terms of partial waves with definite values of orbital angular momentum, just as any MO can be formally expressed as a superposition of atomic orbitals localized on any chosen center. The greatest conceptual insight is often gained when the expansion is carefully chosen so that it is dominated by few leading terms that capture the essential physics.

LCAO: linear combination of atomic orbitals

HOMO: highest-occupied molecular orbital

2.1. Representation of Molecular Orbitals in Atomic Bases

To a chemist, expanding an MO as a linear combination of atomic orbitals (LCAO) resonates with the LCAO-MO theory, which is based on combining the orbitals of different atoms within the molecule. From a pure mathematical standpoint, the basis functions do not have to be associated with any particular atom, nor do they need to be distributed between different centers. The following discussion is based on two theorems that can be stated briefly as follows. First, any well-behaved function f can be expanded in a complete set of linearly independent functions φ_i :

$$f = \sum_i c_i \varphi_i, \quad (2)$$

provided f and all φ_i are defined in the same coordinate space and satisfy the same boundary conditions. Second, all eigenfunctions of a Hermitian operator compose a complete basis set.

Applying these theorems to chemistry, we note that bound MOs are well-behaved functions that asymptotically approach zero for $r \rightarrow \infty$, whereas the atomic orbitals in the usual form $\psi_{n\ell m}(r, \theta, \phi) = R_{n\ell}(r)Y_{\ell m}(\theta, \phi)$ satisfy the same asymptotic condition and are, by definition, eigenfunctions of a Hermitian operator. Hence, $\psi_{n\ell m}$ can be used to expand any bound MO (ψ_{MO}) in the form of Equation 2, with $f = \psi_{\text{MO}}$, $\{\varphi_i\} = \{\psi_{n\ell m}\}$, and the expansion coefficients calculated as the projections of ψ_{MO} on the respective basis functions: $c_{n\ell m} = \langle \psi_{n\ell m} | \psi_{\text{MO}} \rangle$.

The beauty of Equation 2, as applied to MOs, is that it holds regardless of the choice of the Hamiltonian used to generate the expansion basis. The generating Hamiltonian does not have to correspond to any atom in the molecule; its origin and the corresponding atomic orbitals can be placed at any point in the MF. For example, a math enthusiast, unconcerned about physical insight but armed with ample computing power, might choose to represent the $\pi_g^* 2p$ highest-occupied molecular orbital (HOMO) of O_2^- as a combination of unmodified H-atom orbitals with the origin at one of the O atoms. For good measure, one may even instead place the origin a few angstroms (or meters!) away from the O_2^- center of mass. As long as a sufficiently complete $\{\psi_{n\ell m}\}$ set is used and no objection is made to the astronomical length of the expansion, such an unreasonable choice of basis set is formally acceptable.

However, a more insightful approach to this problem is to expand the HOMO in a properly adjusted $\{\psi_{n\ell m}\}$ basis set placed at the O_2^- center of mass. The resulting expansion, although still formally infinite, will contain two dominant terms, corresponding to the $Y_{2, \pm 1}$ spherical harmonics. This description is a mathematical manifestation of the d -like character of the O_2^- HOMO, giving an important insight into its properties, as well as the photodetachment process. In the context of photodetachment, representing the parent MOs in terms of atomic-like functions with common origin is useful because the photodetachment process can then be described as a superposition of channels with defined angular momentum quantum numbers. In the above O_2^- example, one expects the photodetachment to be dominated by the $d \rightarrow p$ and $d \rightarrow f$ channels (in accordance with the $\Delta\ell = \pm 1$ selection rule).

2.2. Partial-Wave Expansion of Continuum Electrons

In a closely related approach, one may choose to use Equation 2 to expand the continuum electron wave function, rather than the parent MO, in the basis of partial waves. This approach is useful even for complex orbitals, for which no effective or dominant ℓ values can be assigned. In such cases, group theory and dipole selection rules are used to determine the symmetry of the continuum wave function, which can then be expanded in a symmetry-adapted partial-wave basis (57). Although plane waves or spherical waves are commonly used, the latter are more appropriate for the analysis of PADs, as they possess defined angular properties. Similar to bound atomic orbitals,

the continuum spherical waves can be factored into the radial and angular parts, with the radial functions dependent on the final-state interactions. In anion photodetachment, the interaction of the photodetached electron with the neutral core is usually weak, and it is well described by free spherical waves, with the radial parts given by spherical Bessel functions (52, 58, 59).

eKE: electron kinetic energy (ε)

2.3. Anion Detachment Versus Neutral-Molecule Ionization

Many ideas in this review are unique to anion photodetachment because the behavior of photodetachment cross sections is sharply different from the analogous properties of neutral ionization. The scaling of the near-threshold cross sections with energy is dependent on the angular momentum quantum number ℓ and the final-state interaction between the departing electron and the remaining neutral or cation. According to the Wigner law (60), in the limit of small electron kinetic energy (eKE), the anion photodetachment cross section corresponding to channel ℓ scales as

$$\sigma_{\ell} \propto \varepsilon^{\ell+1/2}, \quad (3)$$

where $\varepsilon \equiv \text{eKE}$. This law assumes that for large r , the interaction potential of the departing electron with the remaining neutral drops off faster than $1/r^2$, and the long-range effective potential is therefore dominated by the centrifugal term $\ell(\ell + 1)\hbar^2/2\mu r^2$, where μ is the reduced mass of the electron. Equation 3 does not apply if the long-range effective potential is dominated instead by an actual attraction (or repulsion) between the separating particles. In particular, it does not apply to neutral ionization, in which the long-range Coulomb potential ($\propto 1/r$) supersedes the centrifugal term. Equation 3 also loses its validity in the presence of strong electron-dipole interaction (scaling as $1/r^2$, similar to the centrifugal potential).

Per Equation 3, a typical photodetachment process in the proximity of its threshold is dominated by the smallest allowed ℓ waves (57, 61, 62). For example, in O^- , C^- , and OH^- photodetachment, a sharp ($\sigma_0 \propto \varepsilon^{1/2}$) increase in the cross sections is observed near the threshold, attributed to the s partial waves (57). In O_2^- , however, s waves are strictly forbidden by symmetry, so the threshold behavior is controlled by the slow-rising p partial waves ($\sigma_1 \propto \varepsilon^{3/2}$) (57).

The Wigner law is helpful in understanding anion PADs because it can predict the approximate scaling of the relative cross section with eKE. A common concern about its use over energy ranges of several electron volts is that the law, being a threshold law, is strictly valid only at vanishingly small eKE (57, 60–62). This concern is discussed in Section 4.2.

3. PHOTOELECTRON ANGULAR DISTRIBUTIONS BASED ON THE DOMINANT PARTIAL-WAVE CHARACTER

Although the quantitative modeling of PADs must involve extensive and often unintuitive calculations (8, 13, 14, 63–69), important physical insight can be gained from qualitative or semi-quantitative models. These conceptual approaches, relying mainly on pen and paper (rather than a supercomputer) to interface with the explorer's brain, are the main subject of this review.

One such approach, the s & p partial-wave model, has been illustrated for several molecular anions (for examples, see 11, and references therein). It establishes a qualitative relationship between the expected PADs and the symmetry properties of the corresponding parent MO.

First, the s & p partial-wave model considers the detachment in the MF. Within the one-electron, electric-dipole approximation framework, the model requires that the direct product of the irreducible representations of the free-electron wave function (ψ_f), the dipole operator ($\hat{\mu}$), and the initial bound orbital (ψ_{MO}) is invariant under the symmetry operations of the molecular point group.

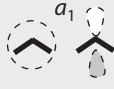
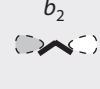
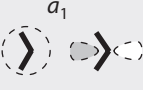
Second, given the allowed symmetries of the free-electron waves, ψ_f is formally expanded in a basis of partial waves with defined ℓ values, emitted from a single center. True to its name, the s & p model limits the consideration to only the $\ell = 0$ and 1 partial waves. This approximation implicitly relies on the effective centrifugal suppression of the higher-order waves, prescribed by the Wigner law (60). Whereas the Wigner law holds only in the immediate proximity of the photodetachment threshold (62), the Wigner-like relative scaling of the partial waves is presumed to persist over a broader (albeit difficult to quantify) energy range (see Sections 2.3 and 4.2).

One may rightly wonder, why limit the discussion specifically to the s and p waves? The model aims to simplify the description of the emitted electrons to the greatest extent possible, while retaining the key physics of the process. This means considering as few partial waves as possible, with the greatest weight always given to the lowest-order waves. Hence, limiting the discussion to just the $\ell = 0$ waves would be tempting but pointless: The s waves are isotropic and by themselves do not give any insight into the actual PAD. Including the anisotropic p waves (which can be polarized in different directions, resulting in different PAD characters) accounts, to the lowest approximation order possible, for the anisotropic nature of the photodetachment, while still maintaining the bare-bones model simplicity.

Next, the emitted s and p waves are referenced from the MF to LF axes. In general, the LF PAD must account for all possible molecular orientations. In the model approach, the PAD's character is determined by considering only few principal orientations of the anion in the LF. This coarse approximation allows us to gain a crude, but intuitive picture of the detachment process.

Table 1 summarizes the application of the s & p partial-wave approach to C_{2v} symmetry anions (11, 24, 45). Each of the three principal LF orientations of the anion frame, shown schematically in the left column, corresponds to one of the molecular axes aligned along the laser polarization direction (z_{LF}), which is presumed vertical. For each orientation, only the transitions

Table 1 The s & p model treatment of the photodetachment of a C_{2v} symmetry anion

Anion orientation ^a	Active μ component ^b	Transition ^c : (Parent MO symmetry) ⁻¹			
		a_1^{-1}	b_1^{-1}	b_2^{-1}	a_2^{-1}
	a_1				a_2 $\ell \geq 2$
	b_1			a_2 $\ell \geq 2$	
	b_2		a_2 $\ell \geq 2$		
Partial-wave characters:		\circ (1), \parallel (3)	\circ (1), \perp (2)	\circ (1), \perp (2)	\perp

^aPrincipal anion orientations.

^bSymmetries of the transition-dipole components driven by laser radiation polarized along the laboratory-frame z axis.

^cThe shaded area indicates the symmetries and s and p partial waves (shown as dashed contours) of the emitted electrons corresponding to the respective transitions and principal orientations.

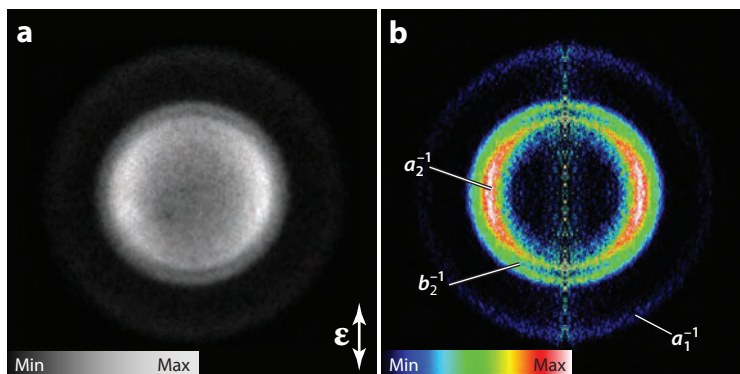


Figure 1

Photoelectron imaging results for CS_2^- at 267 nm linearly polarized along the vertical direction, as indicated by the double arrow in panel *a*. (*a*) The raw photoelectron image integrated over 30,000 laser pulses. (*b*) The Abel-inverted image obtained from the raw image in panel *a*, shown on a color intensity scale. The bands in the Abel-inverted image are labeled in accordance with the molecular orbitals from which the electrons originated.

that possess nonzero dipole components along z_{LF} are active. The MF symmetry species of the active dipole components are indicated in the second column, and the shaded columns list the orientation-dependent symmetries of the emitted electron, determined in the MF by requiring $\langle \psi_f | \hat{\mu} | \psi_{\text{MO}} \rangle \neq 0$. The procedure is repeated for photodetachment from MOs corresponding to each of the four irreducible representations of the point group.

Thus determined symmetry species of the emitted electron waves limit the allowed components of the partial-wave expansion of ψ_f . Whereas *s* waves always correspond to the totally symmetric representation (a_1), *p* waves, depending on their polarization in the MF, can transform as a_1 , b_1 , or b_2 symmetry species. The dashed contours in **Table 1** illustrate the allowed *s* and *p* components of ψ_f . For free-electron waves transforming as a_1 , both *s* and *p* components are allowed. Because the *s* waves are isotropic, their MF \rightarrow LF transformation is trivial. Conversely, the LF polarization of the a_1 symmetry *p* waves is determined by a combination of their MF symmetry and the corresponding anion orientation. Among the b_1 and b_2 symmetry partial waves, only *p* components are allowed in the *s&p* model (i.e., no *s* partial waves). For a_2 waves, the smallest allowed ℓ correspond to *d* waves; therefore, a_2 symmetry partial waves are completely neglected under the model approximation.

Detailed discussions of the benchmark application of the *s&p* partial-wave model to a C_{2v} anion (CS_2^-) can be found in References 11, 24, and 45. Summarizing these discussions, **Figure 1a,b** presents the key results of a photoelectron imaging study of CS_2^- (24), with the 267-nm photoelectron image and its Abel inversion (70), respectively. The three clearly perceptible rings in the image correspond to electrons originating from three distinct MOs, of a_1 , b_2 , and a_2 symmetry.

Considering the wave sketches in the shaded part of **Table 1**, one can clearly see the qualitative nature of the expected PADs. For the a_1^{-1} transition, the free-electron waves are characterized by interference of isotropic *s* waves (\circ anisotropy character in **Table 1**), and *p* waves polarized along z_{LF} (\parallel character). Thus, a predominantly parallel PAD ($\beta > 0$) is expected, in agreement with the properties of the outermost photoelectron band in **Figure 1**. For the b_2^{-1} transition, the model predicts two principal *p* waves with amplitudes peaking perpendicular to the laser polarization (\perp character), as well as an isotropic (\circ character) *s* wave. Overall, $\beta < 0$ is expected, as is indeed observed in the experiment. For the a_2^{-1} transition, the $\ell = 0$ components of ψ_f are forbidden under the electric-dipole approximation, and only horizontally polarized (\perp character) *p* waves

are considered under the *s&p* approximations. A substantially negative value of β (more negative than in the b_2^{-1} case) is therefore predicted and is indeed observed.

The above application of the *s&p* partial-wave model to CS_2^- makes use of the specific properties of the C_{2v} point group. Similar applications to other C_{2v} species, such as dicarboxylate anions, NH_2^- , and carbenes, are discussed in References 11, 29, 71, and 72. Although the C_{2v} group provides the most insightful illustrations of the *s&p* partial-wave approach, applications to other groups are also straightforward. The reader is referred to References 24 and 73–75 for C_s , $D_{\infty h}$, and other examples. In the particular case of diatomics [e.g., O_2^- (73), S_2^- (24), and NO^- (74)], the model has been compared to the Cooper-Zare model (8, 67, 76) adapted to molecular anions (24). To this end, the *s&p* partial-wave model offers the pedagogical advantage of the ease of visualization.

4. THE CENTRAL POTENTIAL MODEL

4.1. The Cooper-Zare Equation

If the initial state of the electron is described by a definite value of ℓ , as in the case of atomic species, the emitted electrons are represented by superpositions of the dipole-allowed partial waves with $\ell_f = \ell \pm 1$. According to the derivations by Bethe and colleagues (77), generalized by Cooper & Zare (67, 76), the anisotropy parameter β for photoemission using linearly polarized light in this case is given by the Cooper-Zare equation:

$$\beta = \frac{\ell(\ell-1)\chi_{\ell,\ell-1}^2 + (\ell+1)(\ell+2)\chi_{\ell,\ell+1}^2 - 6\ell(\ell+1)\chi_{\ell,\ell+1}\chi_{\ell,\ell-1}\cos(\delta_{\ell+1} - \delta_{\ell-1})}{(2\ell+1)[\ell\chi_{\ell,\ell-1}^2 + (\ell+1)\chi_{\ell,\ell+1}^2]}, \quad (4)$$

where $\chi_{\ell,\ell\pm 1}$ are the radial matrix elements for the $\ell_f = \ell \pm 1$ partial waves, and $(\delta_{\ell+1} - \delta_{\ell-1})$ is the phase shift induced by interaction with the remaining neutral (or cation).

A direct application of the Cooper-Zare formula requires the evaluation of radial transition matrix elements, which is not a trivial undertaking in its own right (57). Hanstorp et al. (78) proposed a practical simplification of the problem, assuming that the relative scaling of the partial-wave cross sections follows the Wigner law (60).

4.2. Hanstorp's Formulation of the Cooper-Zare Equation

The Cooper-Zare equation (Equation 4) can be rearranged to show that β is dependent not on the matrix elements themselves, but on the ratio of $\chi_{\ell,\ell+1}$ to $\chi_{\ell,\ell-1}$. In anion photodetachment, this ratio is expected to vary approximately linearly with eKE, ε . This simplification, originally noted by Hanstorp et al. (78), follows from the Wigner law for near-threshold photodetachment (Equation 3), as the partial cross sections are proportional to the squares of the corresponding matrix elements, $\sigma_{\ell\pm 1} \propto \chi_{\ell,\ell\pm 1}^2$.

A common criticism concerning the use of the Wigner law proportionality over energy ranges spanning several electron volts is that the law, being a threshold law, is strictly valid only at vanishingly small kinetic energies (57, 60–62). However, decades of successful and diverse applications of Hanstorp et al.'s approach suggest that, although the Wigner law predictions of partial-wave cross sections are not accurate outside the threshold regime, the law's predictions of cross-section ratios are more robust (14, 15, 24, 38, 47, 74, 79–89). A more detailed discussion of the range of validity of Wigner partial-wave ratios can be found in the online supplement to Reference 52.

Assuming $\sigma_{\ell+1}/\sigma_{\ell-1} \propto \varepsilon^2$, and therefore $\chi_{\ell,\ell+1}/\chi_{\ell,\ell-1} = A_\ell\varepsilon$, where A_ℓ is a proportionality coefficient with units of reciprocal energy, one can arrange Equation 4 to allow the calculation of

β as an explicit function of ε (78):

$$\beta(\varepsilon) = \frac{\ell(\ell - 1) + (\ell + 1)(\ell + 2)A_\ell^2\varepsilon^2 - 6\ell(\ell + 1)A_\ell\varepsilon \cos(\delta_{\ell+1} - \delta_{\ell-1})}{(2\ell + 1)[\ell + (\ell + 1)A_\ell^2\varepsilon^2]}. \quad (5)$$

We refer to this result as Hanstorp et al.'s formulation of the Cooper-Zare equation. Because the Cooper-Zare equation is based on the original derivations by Bethe and colleagues (77), whereas the approximation made by Hanstorp et al. (78) follows from the Wigner law (60), Equation 5 is also sometimes referred to as the Wigner-Bethe-Cooper-Zare equation (51).

Equations 4 and 5 are generally not applicable to molecular anions, for which ℓ is not a good quantum number. In some cases, if the MO resembles an atomic-like orbital, one may, with caution, use an effective ℓ value in Equation 4. For example, the π_g^*2p HOMO of O_2^- , discussed in Section 2.1, is a d -like function, and the photodetachment of O_2^- can be modeled using Equation 5 with $\ell = 2$ (57, 73, 87). However, most MOs cannot be assigned effective ℓ values, as any adequate description of their angular dependence must include several spherical harmonics with different values of ℓ .

4.3. Photodetachment from s and p Orbitals

The simplest case of s orbital photodetachment has been described in detail using the example of H^- (45, 50, 90). A sample photoelectron image of H^- (50) is shown in **Figure 2**. With $\ell = 0$, Equations 4 and 5 do not apply in a rigorous sense, as the $(\ell - 1)$ partial wave and its phase do not exist in this case. However, formally substituting $\ell = 0$ into either Equation 4 or 5 leads to zeroing out the nonexistent terms and yields a simple—and correct—result: a parallel photodetachment with $\beta = 2$, independent of eKE, corresponding to the red pure s limit in **Figure 2**.

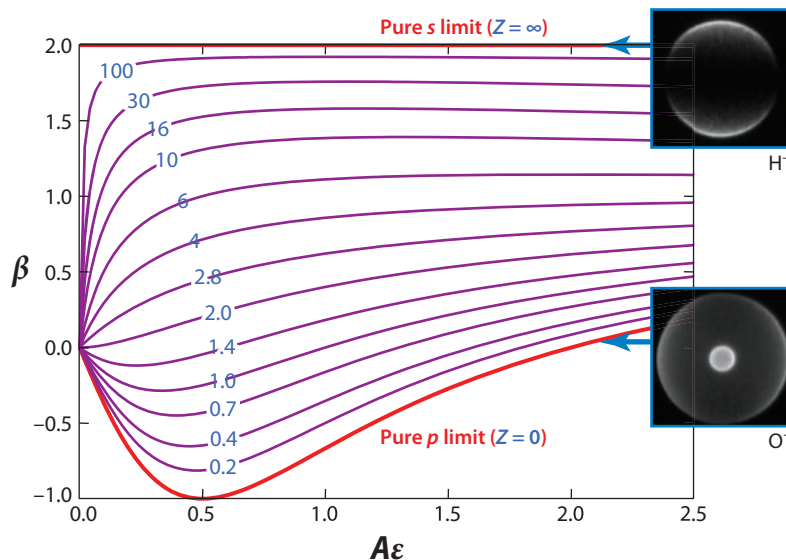


Figure 2

Dependence of the anisotropy parameter β on electron kinetic energy scaled to the size of the parent orbital (i.e., β versus $A\varepsilon$). For example, if $A = 1 \text{ eV}^{-1}$, the horizontal axis corresponds to ε in electron volts. The purple curves are calculated using Equation 13 for the photodetachment from mixed s - p states with different values of the parameter Z , defined by Equation 14, as indicated. The range of the curves shown is from $Z = 0$ (p orbital limit) to ∞ (s orbital limit). Zero phase shift is assumed [i.e., $\cos(\delta_2 - \delta_0) = 1$]. The photoelectron images on the right correspond to H^- and O^- photodetachment, respectively (50).

This result can be obtained in a more physically meaningful way. The electric-dipole selection rule for one-photon detachment from an s orbital with linearly polarized light dictates that the emitted electron is a p wave polarized in the same direction as the detaching radiation (LF z axis). The angular dependence of this p_z wave is described by one spherical harmonic, $Y_{1,0}(\theta, \phi) = (3/4\pi)^{1/2} \cos\theta$, which corresponds to a $\cos^2\theta$ PAD ($\beta = 2$).

In the particular case of photodetachment from a p atomic orbital [see, e.g., the sample O⁻ photoelectron image (50) in **Figure 2**], the interference of s and d partial waves must be considered. With $\ell = 1$, Equation 5 simplifies to

$$\beta(\varepsilon) = \frac{2A^2\varepsilon^2 - 4A\varepsilon \cos(\delta_2 - \delta_0)}{1 + 2A^2\varepsilon^2}, \quad (6)$$

where $A \equiv A_1$ (78). Throughout this review, A without a subscript corresponds to detachment from a p orbital and describes the relative scaling of the radial dipole integrals corresponding to the $p \rightarrow d$ and $p \rightarrow s$ photodetachment channels. One can determine its value by fitting Equation 6 to experimental data. However, it is also possible to obtain an estimate of A from first principles.

Assuming no interaction with the remaining neutral and representing the continuum electron by free spherical waves, the A coefficient is given by the following equation (52):

$$A\varepsilon = \frac{\chi_{1,2}}{\chi_{1,0}} = \frac{\int_0^\infty j_2(kr)r^3 R_{np}(r)dr}{\int_0^\infty j_0(kr)r^3 R_{np}(r)dr}, \quad (7)$$

where $R_{np}(r)$ is the radial part of the initial np orbital (with n the principal quantum number), and $j_0(kr)$ and $j_2(kr)$ are the spherical Bessel functions describing the radial parts of the s and d partial waves, with k the linear momentum wave number, $k = p/\hbar$.

Thus defined parameter A is generally not a constant, as both integrals in Equation 7 are k and therefore ε dependent (52). To make Equation 7 consistent with the use of A as a constant in Equation 6 (and, more generally, Equation 5), we must adopt the same approximation, as in the work of Hanstorp et al. (78), namely the Wigner-like slow-electron limit. In this limit, the de Broglie wavelength of the emitted electron significantly exceeds the radial extent of the bound orbital, and the spherical Bessel functions in Equation 7 can be approximated by the leading (origin) terms of their respective Taylor (Maclaurin) series expansions for $kr \ll 1$. Equation 7 then simplifies to

$$A\varepsilon = \frac{k^2 \int_0^\infty r^5 R_{np}(r)dr}{\int_0^\infty r^3 R_{np}(r)dr}, \quad (8)$$

or, because $\varepsilon = k^2/2$ (in atomic units),

$$A = \frac{2 \int_0^\infty r^5 R_{np}(r)dr}{15 \int_0^\infty r^3 R_{np}(r)dr}. \quad (9)$$

A defined by Equation 9 is indeed independent of energy. Its value is determined exclusively by the radial moments of the bound orbital.

The r^3 and r^5 factors under the integrals in Equation 9 imply that parameter A is particularly sensitive to the long-range behavior of the bound orbital. This observation justifies describing the initial state with a standard hydrogenic function, defined by the principal quantum number n and effective nuclear charge ζ_{np} . Then, both integrals in Equation 9 can be evaluated analytically. For the particular case of photodetachment from a $2p$ orbital (52),

$$A = \frac{16}{5^2_{2p}} \text{Hartree}^{-1} \approx (0.588/\zeta_{2p}^2) \text{ eV}^{-1}. \quad (10)$$

This approximate prediction can be compared directly to the experimental results for second-row anions. For example, the value of A determined by fitting Equation 6 to experimental anisotropy data for O^- is $A = 0.55 \pm 0.045 \text{ eV}^{-1}$ (38, 78, 89, 91, 92). This result is consistent with Equation 10, assuming $\zeta_{2p} \approx 1$. To put this effective charge in perspective, let us compare it, on the one hand, to the prediction of Slater's rules (93, 94) of $\zeta_{2p} = 4.2$ for O^- . On the other hand, let us recall that the determining role in the calculation of A belongs to the diffuse long-range tail of the anionic wave function, not the core part that Slater's rules are designed to describe. The long-range tail interacts with a nearly neutral core, asymptotically corresponding to $\zeta_{2p} \rightarrow 0$ as $r \rightarrow \infty$. The above value of $\zeta_{2p} \approx 1$ is a reasonable compromise between 0 and 4.2.

Understanding C^- PADs is an important step in modeling the photodetachment of organic anions. Although the electron affinity of atomic carbon is well known (1.262 eV) (95), limited data exist for the corresponding PADs (81, 91, 96). Modeling the available $C^- (^4S)$ results with Equation 6 yields $A \approx 0.75 \text{ eV}^{-1}$ (52). As pointed out by Hanstorp et al. (78) and evident from Equation 9, A reflects the spatial extent of the anion wave function. The larger value of A for C^- (0.75 eV^{-1}), compared to that for O^- (0.55 eV^{-1}), is consistent with the relative sizes of these anions.

5. PHOTODETACHMENT FROM s - p MIXED-CHARACTER STATES

Until recently, no practical analog of the Cooper-Zare formula existed for photodetachment from MOs described by more than one ℓ value (97). Concepts similar to those that underlie the $s\&p$ partial-wave approach (Section 3) have led to an approximate formalism for photodetachment from mixed-character s - p states. Initially proposed by Grumbling (98), the mixed s - p model is applicable to PADs resulting from a broad class of hybrid orbitals (52, 54), as well as some solvation-polarized initial states (51). Although the mixed s - p model is similar in name to the $s\&p$ partial-wave model, the two approaches are different and should not be confused.

The mixed s - p model applies to hybrid orbitals localized predominantly on a single central atom in a molecule. Such systems are ubiquitous in chemistry, but one limitation of the mixed s - p model is its reliance on the central-atom approximation.

5.1. Model Approximations and Formalism

The mixed s - p model considers photodetachment from a state represented as a linear combination of one s - and one p -type function localized on the same center in the MF (51):

$$|\psi_{sp}\rangle = \sqrt{1-f}|s\rangle + \sqrt{f}|p\rangle, \quad (11)$$

where f is the fractional p character, $0 \leq f \leq 1$. Any relative phase factors are absorbed into the corresponding kets. Equation 11 can be used to approximate canonical Hartree-Fock orbitals, or without much extra effort or loss of generality, the same approach can be applied to Dyson orbitals (14, 15, 99).

In the electric-dipole approximation, photodetachment from a mixed state described by Equation 11 yields s , p , and d partial waves via the $s \rightarrow p$ and $p \rightarrow s, d$ channels. Similar to Hanstorp et al. (78) (Section 4.2), the model assumes the Wigner-like (60) scaling of the partial-wave cross sections. Namely, $\chi_{1,2}^2/\chi_{1,0}^2 = A^2 \varepsilon^2$ and $\chi_{0,1}^2/\chi_{1,0}^2 = B\varepsilon$, where $\chi_{\ell,\ell\pm 1}$ are the radial dipole elements for the $\ell \rightarrow \ell \pm 1$ photodetachment channels. A is the same model parameter describing the relative scaling of the $p \rightarrow d$ and $p \rightarrow s$ channels discussed in Section 4.3, and B is a hallmark of the mixed s - p model, describing the relative scaling of the $s \rightarrow p$ and $p \rightarrow s$ channels.

Under these assumptions, the anisotropy parameter β is an explicit function of eKE (51):

$$\beta(\varepsilon) = \frac{2(1-f)B\varepsilon + 2fA^2\varepsilon^2 - 4fA\varepsilon \cos(\delta_2 - \delta_0)}{(1-f)B\varepsilon + 2fA^2\varepsilon^2 + f}. \quad (12)$$

This result differs from the Cooper-Zare model (Equation 5) in that it describes photodetachment from a mixed s - p orbital, rather than a state with a defined ℓ value. In the limiting cases of $f = 0$ and 1, Equation 12 reduces exactly to the respective Cooper-Zare predictions for detachment from pure s and pure p states. Thus, both limits of the mixed s - p model are consistent with the Cooper-Zare central potential formula. For mixed states ($f \neq 0$), one can rearrange Equation 12 as follows:

$$\beta(\varepsilon) = \frac{2ZA\varepsilon + 2(A\varepsilon)^2 - 4A\varepsilon \cos(\delta_2 - \delta_0)}{ZA\varepsilon + 2(A\varepsilon)^2 + 1}, \quad (13)$$

where a new parameter Z is introduced (52), defined as

$$Z = \frac{1-f}{f} \frac{B}{A}. \quad (14)$$

Thus, aside from the phase shift, the model anisotropy trends $\beta(\varepsilon)$ are determined by two parameters, A and Z , rather than three (A , B , and f), as may appear from Equation 12. The meaning of the new parameter Z is transparent: It describes the relative intensities of the $s \rightarrow p$ and $p \rightarrow s$, d channels (via B/A), weighted by the contributions of the s and p components to the initial state, $(1-f)/f$. The pure p state limit ($f = 1$) corresponds to $Z = 0$, whereas for a pure s state ($f = 0$), $Z \rightarrow \infty$.

Similar to the many applications of the Cooper-Zare equation, the s - d phase shift in Equations 12 and 13 can be either presumed small or neglected altogether by setting $\cos(\delta_2 - \delta_0) = 1$. This approximation is reasonably justified for the electrons that interact weakly with the remaining neutral core, and a large phase shift between the s and d partial waves is not expected.

Neglecting the phase shift, the Z parameter (Equation 14) contains all the physics and chemistry of the process (within the model constraints) by combining the relative channel cross sections with the properties of the parent MO. Furthermore, Equation 13 reveals that for a given value of Z , the anisotropy parameter is a unique function of $A\varepsilon$, rather than ε . Hence, if the energy scale is properly normalized with regard to the size of the initial orbital (as determined by A ; see Section 4.3), the corresponding anisotropy trend is completely determined by Z . This is illustrated in **Figure 2**, which plots the anisotropy parameter β , as determined by Equation 13, versus $A\varepsilon$ for different Z values, ranging from $Z = 0$ (p orbital limit) to ∞ (s orbital limit). This plot is a summary of the mixed s - p model results (51), applicable to photodetachment from any such mixed-character anionic state.

5.2. Evaluation of the Model Parameters

The Z value describing the photodetachment process for mixed s - p states is a composite parameter (per Equation 14). Its evaluation requires the knowledge of the B/A ratio and the fractional p character (f) of the parent orbital. In this section, we outline the ab initio procedures that can be used to evaluate these properties.

5.2.1. The B/A ratio. The B/A ratio depends on the types of the s and p components of the parent hybrid orbital, $n's$ and np . The prime in $n's$ indicates that the s and p components of the initial state do not have to correspond to the same principal quantum number. (For example, in Section 5.3.2, the solvation-induced polarization of H^- is described by a small $2p$ contribution added to the $1s$ orbital; i.e., $n' = 1$ and $n = 2$.)

Formally, B/A is defined as the ratio of the $s \rightarrow p$ to $p \rightarrow d$ and $p \rightarrow s$ to $s \rightarrow p$ relative transition amplitudes (52). Under assumptions similar to those underlying Equation 7 (no interaction of the

continuum electron with the remaining neutral), the B/A ratio is given by

$$\frac{B}{A} = \frac{\left(\int_0^\infty j_1(kr)r^3 R_{n's}(r)dr\right)^2}{\int_0^\infty j_0(kr)r^3 R_{np}(r)dr \int_0^\infty j_2(kr)r^3 R_{np}(r)dr}, \quad (15)$$

where $R_{n's}(r)$ and $R_{np}(r)$ are the radial parts of the s and p components of the initial $n's$ - np orbital, and $j_\ell(kr)$ are the spherical Bessel functions describing the radial parts of the emitted waves. In a manner similar to Equation 9, if the de Broglie wavelength of the emitted electron significantly exceeds the radial extent of the bound orbital, one can replace the spherical Bessel functions with their origin terms, simplifying Equation 15 to

$$\frac{B}{A} = \frac{5}{3} \frac{\left(\int_0^\infty r^4 R_{n's}(r)dr\right)^2}{\int_0^\infty r^3 R_{np}(r)dr \int_0^\infty r^5 R_{np}(r)dr}. \quad (16)$$

Despite the explicit k dependence of the integrals in Equation 15, the B/A ratio in Equation 16 is independent of k and therefore ε . This result is consistent with the Wigner law (60) and the formulations by Hanstorp et al. (78).

Just as the r^3 and r^5 factors under the integrals in Equation 9 make A sensitive mostly to the long-range tails of the bound orbital, the r^3 , r^4 , and r^5 factors under the integrals in Equation 16 impose the same sensitivity on B/A . The s and p components of the orbital can therefore be approximated by the corresponding hydrogenic functions, defined by the principal quantum numbers n' and n and effective nuclear charges $\zeta_{n's}$ and ζ_{np} , respectively. With this approximation, all integrals in Equation 16 can be evaluated analytically using a pen and paper only (52), giving the B/A ratio for the specific $n's$ - np mixing case.

In the particularly important case of $2s$ - $2p$ mixing (relevant to photodetachment from a broad class of sp^n hybrid orbitals of organic compounds), the result is (52)

$$\frac{B}{A} = \frac{8}{3} \left(\frac{\zeta_{2p}}{\zeta_{2s}}\right)^7. \quad (17)$$

Under the further approximation of equal $2s$ and $2p$ effective nuclear charges, Equation 17 simplifies further to $B/A = 8/3$. The $\zeta_{2p} = \zeta_{2s}$ assumption may look suspicious in view of the different core-penetration properties of the $2s$ and $2p$ functions. This suspicion is further amplified by the seventh-power dependence of B/A on ζ_{2p}/ζ_{2s} in Equation 17. Nonetheless, the assumption is consistent with the dominant role of the tails of anion orbitals in determining the detachment regime. The effective charge in the mixed s - p model is intended to describe these very diffuse tails, rather than the divergent degrees of core penetration. As the $2s$ and $2p$ tails interact with a similarly charged core, the assumption $\zeta_{2p} = \zeta_{2s}$ is justified, to a degree.

Calculations for other ns - np ($n = n'$) mixing cases show that B/A varies with n . Assuming, again, $\zeta_{ns} = \zeta_{np}$, we obtain $B/A = 121/60$ for the $3s$ - $3p$ mixing, $B/A = 24/13$ for $4s$ - $4p$, $B/A = 135/76$ for $5s$ - $5p$, etc. These fractions are plotted as a function of n in **Figure 3** and are easily generalized, similar to Equation 17, for mixed states with $\zeta_{ns} \neq \zeta_{np}$. As n increases in **Figure 3** (e.g., for Rydberg-like dipole-bound states), B/A approaches the asymptotic limit of $5/3$.

Similar calculations have been carried out for the off-diagonal (i.e., $n' \neq n$) $n's$ - np cases. For example, in the $1s$ - $2p$ scenario, relevant to the perturbation of H^- by solvation (see Section 5.3.2), $B/A = (1/768)(\zeta_{2p}/\zeta_{1s})^7$ (51, 71). The assumption $\zeta_{1s} = \zeta_{2p}$ would not be appropriate (even approximately) in this case, as $\zeta_{1s} > \zeta_{2p}$ is expected, owing to the very diffuse nature of the solvation-induced polarization component.

5.2.2. Fractional p character. The mixed s - p model formally considers photodetachment from MOs localized on a single central atom. The parameter f in Equations 11, 12, and 14 describes

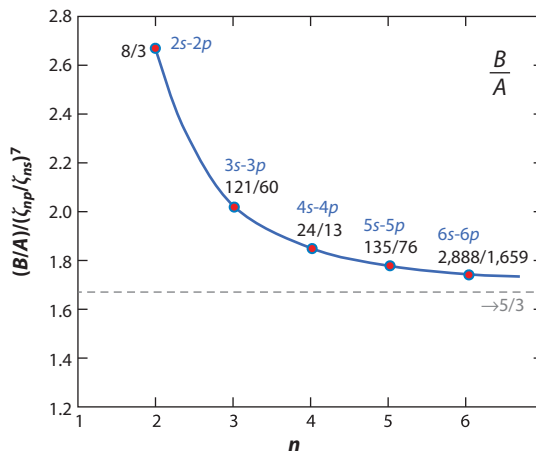


Figure 3

The B/A ratios for different ns - np mixing cases calculated by substituting the corresponding hydrogenic orbitals into Equation 16. The continuous curve is intended as a guide. The fractions indicated next to the data points correspond to equal ns and np effective charges, $\zeta_{ns} = \zeta_{np}$. For $\zeta_{ns} \neq \zeta_{np}$, the B/A ratios are equal to the indicated fractions multiplied by $(\zeta_{np}/\zeta_{ns})^7$. Figure reprinted with permission from Reference 52. Copyright 2013 AIP Publishing LLC.

the fractional p character of the specific detachment orbital, rather than the bonding character of the atom (as related to bond angles).

One approach to quantifying the p character is based on analyzing the ab initio MO coefficients for the s - and p -type functions of (only) the central atom. For example, for a nominal sp^2 hybrid orbital, not accounting for contributions from the neighboring atoms, $f = 2/3$. This approach is appealing, on its surface, because of the intuitive link to the canonical hybridization state of the atom's orbitals. Its drawback mirrors the limitation of the central-atom approximation. Molecular-anion photodetachment involves MOs, rather than the orbitals of just the central atom. This holds true even for canonical nonbonding orbitals (52).

A more successful approach to determining the value of f involves directly fitting a mixed s - p model function to an ab initio parent MO (which can be a canonical Hartree-Fock or Dyson orbital) (54). This approach amounts to representing the MO in the mixed s - p basis that consists of only two functions. Specifically, one constructs a model orbital ψ_{sp} as a superposition of hydrogenic s and p functions (one of each), per Equation 11. The spatial extent of the components is described by effective nuclear charge ζ , assumed to be the same for both the s and p contributions (see Section 5.2.1). The model orbital is thus controlled by two parameters, ζ and f , both of which are used to optimize the overlap of ψ_{sp} with the MO determined from ab initio calculations.

5.3. Benchmark Applications of the Mixed s - p Model

We now demonstrate the application of the mixed s - p model in two very different regimes. First is the photodetachment from sp^x hybrid orbitals with sizable contributions of both s and p functions. Second is the photodetachment from an atomic-anion orbital merely perturbed by solvation.

5.3.1. Hybrid orbitals. An application of the model to polyatomic organic anions has been recently illustrated using pyridinide ($C_5H_4N^-$) as a model system (54). This closed-shell anion is derived from deprotonation of pyridine, C_5H_5N , at the C4 position (100, 101). The dominant

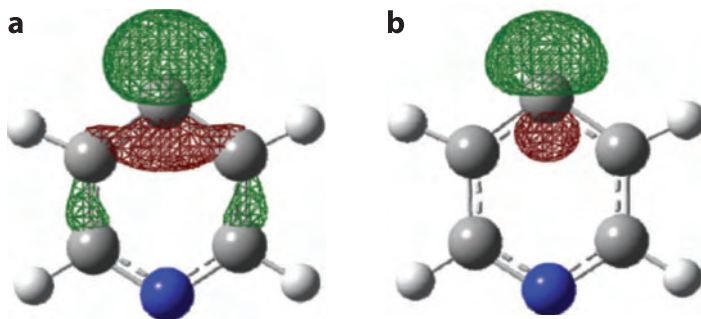


Figure 4

(a) The ground-state geometry and the HOMO of the pyridinide anion, $C_5H_4N^-$ (54). (b) The model wave function obtained as a least-squares fit of ψ_{sp} defined in the text to the ab initio orbital shown in panel a. Figure reprinted with permission from Reference 54. Copyright 2013 American Chemical Society.

contribution to the HOMO (**Figure 4a**) results from the in-plane hybridized (nominally) sp^2 orbital of the deprotonated carbon center.

Figure 5 shows the eKE-dependent β values observed in $C_5H_4N^-$ photodetachment (54). The values follow a clear trend, which is analyzed here for comparison, within two different conceptual frameworks: (a) by representing the $C_5H_4N^-$ HOMO as a p -like function within the Cooper-Zare central potential model and (b) by treating the HOMO, more appropriately, as a hybrid orbital within the mixed s - p model.

Curve 1 in **Figure 5** was calculated using the Cooper-Zare equation for $\ell = 1$ (Equation 6), neglecting the phase shift between the s and d partial waves. The calculation captures the

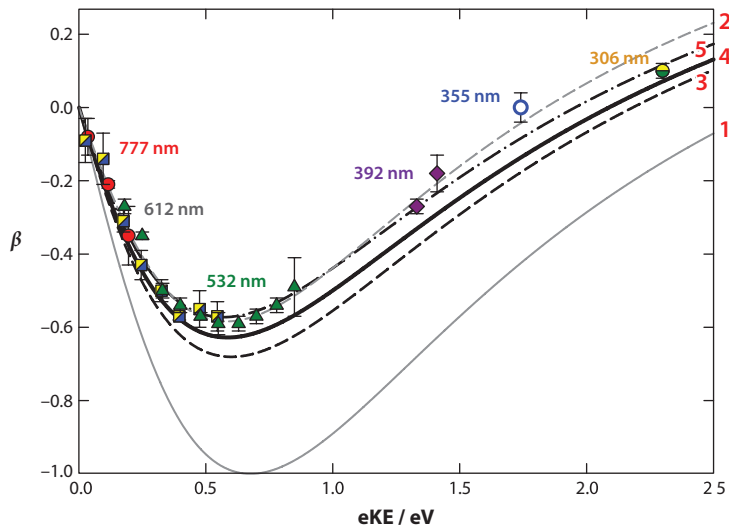


Figure 5

Experimental photoelectron anisotropy parameter values (*symbols*) resulting from pyridinide photodetachment plotted versus electron kinetic energy (54). Model curves are numbered along the right. Curves 1 and 2 are derived from the Cooper-Zare central potential model (Equation 5) with $\ell = 1$ and $A = 0.75 \text{ eV}^{-1}$. Curves 3–5 are mixed s - p model predictions (Equations 13 and 14), assuming $A = 0.75 \text{ eV}^{-1}$, $B/A = 8/3$, and parameter values discussed in the text. Figure reprinted with permission from Reference 54. Copyright 2013 American Chemical Society.

approximate location of the minimum in the experimental $\beta(\varepsilon)$ dependence, but its overall agreement with the experiment is poor. In particular, the depth of the minimum, determined solely by the phase shift within the Cooper-Zare model, is not reproduced even approximately. Using the phase shift as an adjustable parameter and fitting Equation 6 to the measured $\beta(\varepsilon)$ values, one yields curve 2. The fit is in good agreement with the data but requires a very large, unphysical phase shift, $\cos(\delta_2 - \delta_0) = 0.68$. This outcome is not surprising, as the $C_5H_4N^-$ HOMO is hardly a simple p orbital.

A more appropriate, yet still conceptually straightforward approach is to treat the HOMO as an s and p hybrid orbital. The addition of partial s character to the model description of the anion HOMO opens the p detachment channel, not accounted for by the above application of the Cooper-Zare model. To determine the fractional p character of the hybrid state, one constructs a model orbital ψ_{sp} , defined as a superposition of hydrogenic $2s$ and $2p$ functions on the deprotonated carbon center in $C_5H_4N^-$ and then fits it to the HOMO of $C_5H_4N^-$ shown in **Figure 4a**. This procedure is purely ab initio in nature, independent of the experimental results; it is not a model fit to the data. The fit yields $\zeta = 3.10$ and $f = 0.88$. The effective charge of 3.10 compares favorably to the predictions of Slater's rules (93) of 3.25 and 2.9 for the $n = 2$ electrons in C and C^- , respectively. As the excess charge in the pyridinide anion is partially delocalized, the ζ value is indeed expected to be intermediate between those for the atomic neutral and the singly charged anion. **Figure 4b** plots the optimized model orbital. As expected, the model orbital correctly captures the hybrid character of the dominant part of the HOMO centered on C4, while missing the delocalized parts of the orbital.

The above fractional p character value $f = 0.88$ does not reflect just the hybridization state of the C4 atom in pyridinide. This value is determined by fitting the model orbital to the ab initio HOMO, including the contributions of the neighboring atoms. Calculating f from the MO coefficients for the s - and p -type functions of C4 only, contributing to the HOMO, one yields a significantly smaller f value of ~ 0.6 . The constructive contributions of the neighboring-atom (C3 and C5) orbitals to the HOMO density just below the C4 center (in the orientation shown in **Figure 4**) have the effect of partially symmetrizing the orbital with respect to C4, thus increasing the effective p character of the model orbital without affecting the intrinsic hybridization state of C4. The $f = 0.88$ value can be said to include a correction for the partial breakdown of the central-atom approximation implicit in the model.

Substituting $f = 0.88$ and $B/A = 8/3$ (see Section 5.2.1) into Equation 14 yields $Z = 0.36$. Assuming no phase shift, this Z value, together with $A = 0.75 \text{ eV}^{-1}$ (52) for carbon-based anionic $2p$ orbitals, allows one to model the eKE dependence of the anisotropy parameter using Equation 13. The resulting $\beta(\varepsilon)$ prediction is plotted in **Figure 5** as curve 3. It is in nearly quantitative agreement with the experimental results.

Further improvement of the model can be achieved by taking into account the electron correlation and relaxation effects inherent in the photodetachment of the many-electron system. To this end, without much additional effort, one can replace the canonical Hartree-Fock HOMO used in the above analysis with the corresponding Dyson orbital (14, 15, 99) computed (102) using the EOM-IP-CCSD method (103). The resulting model function ψ_{sp} with the optimized parameter values $f = 0.86$ and $\zeta = 3.13$ is very similar to that obtained in the above analysis for the Hartree-Fock orbital. **Figure 5** shows the corresponding model prediction as curve 4.

Curves 3 and 4 in **Figure 5** represent unaltered model predictions, calculated from first principles without any adjustable parameters or fitting to experimental data (unlike the Cooper-Zare fit given by curve 2). The nearly quantitative agreement of curves 3 and 4 with the experimental data suggests that the model correctly captures the physics of the photodetachment process from the hybrid initial state.

Finally, one may question the assumption of a zero phase shift used in the calculations. In many previous attempts to model anion photodetachment using the Cooper-Zare formula, investigators found phase shifts in the range $\cos(\delta_2 - \delta_0) = 0.86\text{--}0.96$ (57, 73, 78, 82, 86, 87). Curve 5 in **Figure 5** was calculated using Equation 13 with the Dyson orbital parameters ($f = 0.86$) and the cosine of the phase shift set arbitrarily to 0.95. The resulting agreement with the experiment is remarkable, but in contrast to curves 3 and 4, curve 5 does include an adjustable parameter (the above cosine), with no solid justification given for the value used.

Applications of the mixed s - p model to other heterocyclic organic anions (55, 104) and other systems (52) have also been demonstrated. In all cases studied, the inclusion of both s and p character of the initial wave function proved crucial for an adequate description of the experimental results.

5.3.2. Solvation-induced polarization within the mixed s - p formalism. The anion orbitals tend to be diffuse, making them particularly sensitive to external perturbations and intermolecular interactions. Here we focus on cases in which one can describe the dominant effect of solvent-induced perturbation of an anion by a single p -type polarization term. In such cases, the $n's\text{-}np$ ($n' \neq n$) mixing variant of the mixed s - p model is applicable. As a specific example, we discuss the adaptation of this approach to $\text{H}^-(\text{NH}_3)_n$ cluster anions (51, 52, 71).

In considering the interaction of the $1s$ electrons of H^- with a single polar solvent molecule, one may approximately describe the resulting perturbation of the anion with a $2p$ function added to the anionic $1s$ orbital. A similar argument holds, approximately, for larger asymmetrically solvated clusters, so we adopt the $1s\text{-}2p$ mixing scenario with a very small fractional p character ($f \ll 1$) to understand the PADs in $\text{H}^-(\text{NH}_3)_n$ photodetachment. Estimating the model parameters is a challenging task in this case because of the difficulty of modeling the perturbed anion orbitals in asymmetric solvent environments, but meaningful physical insight can be gleaned from comparison to experimental data.

As discussed in Section 5.2.1, in the $1s\text{-}2p$ mixing case, $B/A = (1/768)(\zeta_{2p}/\zeta_{1s})^7$, with $\zeta_{2p} \ll \zeta_{1s} < 1$, as mandated by the diffuse nature of the H^- $1s$ orbital and a far more diffuse nature of the solvation-induced polarization component. Considering the seventh-power dependence on ζ_{2p}/ζ_{1s} , a B/A ratio $< 10^{-3}$ can easily be expected.

Figure 6 shows the photoelectron anisotropy data for $\text{H}^-(\text{NH}_3)_n$ cluster anions collected at 532 nm (for $n = 0\text{--}5$), 355 nm ($n = 0\text{--}5$), and 786 nm ($n = 0\text{--}2$) (71). As usual, for a meaningful examination of the electronic-structure or photoelectron-solvent interaction effects, the observed anisotropy parameter values are plotted versus eKE. To understand the role of solvent-induced perturbation on the photodetachment process, one should compare the cluster results to the zero-solvation reference. In the case of unsolvated H^- , it is $\beta = 2$, independent of eKE (see Section 4.3).

Figure 6 indicates the $\beta = 2$ zero-solvation reference for the $\text{H}^-(\text{NH}_3)_n$ cluster series. The experimental results for bare H^- fall close to this limit and indeed do not display an energy dependence, consistent with other measurements for this system (91, 105). In comparison, the $\text{H}^-(\text{NH}_3)_n$, $n > 0$, results exhibit significant deviations from the $\beta = 2$ limit. These solvation-induced deviations are most pronounced at small eKE.

In addition to the zero-solvation unperturbed s orbital limit ($Z = \infty$), **Figure 6** shows two mixed s - p model curves corresponding to $Z = 12$ and 36. The chosen Z values provide effective bounds for the observed experimental $\beta(\epsilon)$ trends, and it is revealing that the data for the smaller clusters ($n = 1$) gravitate toward the upper bound ($Z = 36$), whereas those for the larger clusters ($n = 4, 5$) fall closer to $Z = 12$. Altogether, the model correctly reproduces the striking solvation-induced deviations of β from the zero-solvation limit, particularly at small eKE. Solvation polarizes the diffuse $1s$ orbital of H^- , introducing some p character to the initial state and resulting in the opening of the $p \rightarrow s$ channel. Even for a small perturbation, the isotropic s waves are most

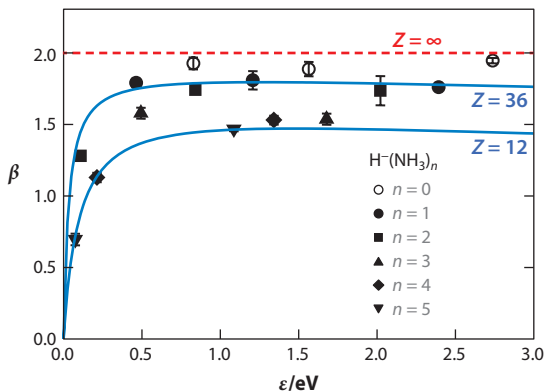


Figure 6

Experimental energy dependence of photoelectron anisotropy parameters for photodetachment from $\text{H}^-(\text{NH}_3)_n$, $n = 0-5$ at 532 and 355 nm and $n = 0-2$ at 786 nm. Lines correspond to predictions of the mixed s - p model predictions (Equations 13 and 14) with the parameter values as indicated and discussed in the text. Experimental data taken from Reference 71.

important at small to moderate $e\text{KE}$ (see Section 2.3), the region where the $\text{H}^-(\text{NH}_3)_n$ PADs deviate most strongly from the zero-solvation limit.

With further development, it should be possible to obtain a quantitative estimate of the ζ_{2p}/ζ_{1s} charge ratio describing the $\text{H}^-(\text{NH}_3)_n$ clusters. With that, one could estimate the B/A ratio, per $B/A(1s-2p) = (1/768)(\zeta_{2p}/\zeta_{1s})^7$. The Z values in **Figure 6** could then be used to calculate the fractional p character of the solvation-polarized H^- orbitals, quantifying the effect of the perturbation of the anion within the clusters. In the absence of such exact estimates, if $B/A < 10^{-3}$ is assumed, a polarization-induced fractional p character $f < 3 \times 10^{-5}$ is indicated by the experimental results.

6. SUMMARY

In stark contrast to neutral-molecule ionization, photodetachment processes at small to moderate $e\text{KE}$ s are dominated by partial waves with the smallest allowed values of angular momentum. This allows for significant simplifications in the qualitative understanding of the process. In one approach, one may draw conclusions about the expected PAD character based on the symmetry-allowed s and p partial waves contributing to the photodetached electron. In a different but related approach, the parent MO can be described based on its dominant s and p contributions, whereas the properties of the continuum electron are determined by the interference of the $s \rightarrow p$ and $p \rightarrow s, d$ photodetachment channels. The analysis of the PADs within this approximate framework reveals the character of the parent orbitals and the essential physics of the photodetachment processes.

DISCLOSURE STATEMENT

The author is not aware of any affiliations, memberships, funding, or financial holdings that might be perceived as affecting the objectivity of this review.

ACKNOWLEDGMENTS

The author is indebted to all the past and present members of the Sanov research group who carried out the original experiments and otherwise contributed to the work cited and described in this

article. I especially thank Emily Rose Grumblin and Lori Marie Culberson for their contributions to the development of the mixed s - p mode. The generous support of the US National Science Foundation (grants CHE-1011895 and CHE-1266152) and the Davis and Weed Endowment is gratefully acknowledged.

LITERATURE CITED

1. Eland JHD. 1984. *Photoelectron Spectroscopy: An Introduction to Ultraviolet Photoelectron Spectroscopy in the Gas Phase*. London: Butterworths
2. Ervin KM, Lineberger WC. 1992. Photoelectron spectroscopy of negative ions. In *Advances in Gas Phase Ion Chemistry*, ed. NG Adams, LM Babcock, pp. 121–66. Greenwich, CT: JAI
3. Chandler DW, Houston PL. 1987. Two-dimensional imaging of state-selected photodissociation products detected by multiphoton ionization. *J. Chem. Phys.* 87:1445–47
4. Heck AJR, Chandler DW. 1995. Imaging techniques for the study of chemical-reaction dynamics. *Annu. Rev. Phys. Chem.* 46:335–72
5. Houston PL. 1995. Snapshots of chemistry: product imaging of molecular reactions. *Acc. Chem. Res.* 28:453–60
6. Ashfold MNR, Nahler NH, Orr-Ewing AJ, Vieuxmaire OPJ, Toomes RL, et al. 2006. Imaging the dynamics of gas phase reactions. *Phys. Chem. Chem. Phys.* 8:26–53
7. Eppink ATJB, Parker DH. 1997. Velocity map imaging of ions and electrons using electrostatic lenses: application in photoelectron and photofragment ion imaging of molecular oxygen. *Rev. Sci. Instrum.* 68:3477–84
8. Cooper J, Zare RN. 1968. Photoelectron angular distributions. In *Atomic Collision Processes*, ed. S Geltman, KT Mahanthappa, WE Brittin, pp. 317–37. New York: Gordon & Breach
9. Seideman T. 2000. Time-resolved photoelectron angular distributions as a means of studying polyatomic nonadiabatic dynamics. *J. Chem. Phys.* 113:1677–80
10. Reid KL. 2003. Photoelectron angular distributions. *Annu. Rev. Phys. Chem.* 54:397–424
11. Sanov A, Mabbs R. 2008. Photoelectron imaging of negative ions. *Int. Rev. Phys. Chem.* 27:53–85
12. Underwood JG, Reid KL. 2000. Time-resolved photoelectron angular distributions as a probe of intramolecular dynamics: connecting the molecular frame and the laboratory frame. *J. Chem. Phys.* 113:1067–74
13. Seideman T. 2002. Time-resolved photoelectron angular distributions: concepts, applications, and directions. *Annu. Rev. Phys. Chem.* 53:41–65
14. Oana CM, Krylov AI. 2007. Dyson orbitals for ionization from the ground and electronically excited states within equation-of-motion coupled-cluster formalism: theory, implementation, and examples. *J. Chem. Phys.* 127:234106
15. Oana CM, Krylov AI. 2009. Cross sections and photoelectron angular distributions in photodetachment from negative ions using equation-of-motion coupled-cluster Dyson orbitals. *J. Chem. Phys.* 131:124114
16. Lawrence EO, Chaffee MA. 1930. On the direction of emission of photoelectrons from potassium vapor by ultraviolet light. *Phys. Rev.* 36:1099–100
17. Stolow A, Bragg AE, Neumark DM. 2004. Femtosecond time-resolved photoelectron spectroscopy. *Chem. Rev.* 104:1719–57
18. Pinaré JC, Baguenard B, Bordas C, Broyer M. 1998. Photoelectron imaging spectroscopy of small clusters: evidence for non-Boltzmannian kinetic-energy distribution in thermionic emission. *Phys. Rev. Lett.* 81:2225–28
19. Baguenard B, Pinaré JC, Bordas C, Broyer M. 2001. Photoelectron imaging spectroscopy of small tungsten clusters: direct observation of thermionic emission. *Phys. Rev. A* 63:023204
20. Deyerl HJ, Alconcel LS, Continetti RE. 2001. Photodetachment imaging studies of the electron affinity of CF_3 . *J. Phys. Chem. A* 105:552–57
21. Surber E, Sanov A. 2002. Photoelectron imaging spectroscopy of molecular and cluster anions: CS_2^- and $\text{OCS}^-(\text{H}_2\text{O})_{1,2}$. *J. Chem. Phys.* 116:5921–24

22. Davis AV, Wester R, Bragg AE, Neumark DM. 2003. Time-resolved photoelectron imaging of the photodissociation of I_2^- . *J. Chem. Phys.* 118:999–1002
23. Peterka DS, Lindinger A, Poisson L, Ahmed M, Neumark DM. 2003. Photoelectron imaging of helium droplets. *Phys. Rev. Lett.* 91:043401
24. Surber E, Mabbs R, Sanov A. 2003. Probing the electronic structure of small molecular anions by photoelectron imaging. *J. Phys. Chem. A* 107:8215–24
25. Mabbs R, Surber E, Sanov A. 2003. Photoelectron imaging of negative ions: atomic anions to molecular clusters. *Analyst* 128:765–72
26. Bragg AE, Wester R, Davis AV, Kammrath A, Neumark DM. 2003. Excited-state detachment dynamics and rotational coherences of C_2^- via time-resolved photoelectron imaging. *Chem. Phys. Lett.* 376:767–75
27. Bragg AE, Verlet JRR, Kammrath A, Neumark DM. 2004. C_6^- electronic relaxation dynamics probed via time-resolved photoelectron imaging. *J. Chem. Phys.* 121:3515–26
28. Verlet JRR, Bragg AE, Kammrath A, Cheshnovsky O, Neumark DM. 2004. Time-resolved relaxation dynamics of Hg_n^- ($11 < n < 16$, $n = 18$) clusters following intraband excitation at 1.5 eV. *J. Chem. Phys.* 121:10015–25
29. Bowen MS, Continetti RE. 2004. Photodetachment imaging study of the vinoxide anion. *J. Phys. Chem. A* 108:7827–31
30. Bragg AE, Verlet JRR, Kammrath A, Cheshnovsky O, Neumark DM. 2005. Time-resolved intraband electronic relaxation dynamics of Hg_n^- clusters ($n = 7-13, 15, 18$) excited at 1.0 eV. *J. Chem. Phys.* 122:054314
31. Rathbone GJ, Sanford T, Andrews D, Lineberger WC. 2005. Photoelectron imaging spectroscopy of $Cu^-(H_2O)_{1,2}$ anion complexes. *Chem. Phys. Lett.* 401:570–74
32. Nee MJ, Osterwalder A, Zhou J, Neumark DM. 2006. Slow electron velocity-map imaging photoelectron spectra of the methoxide anion. *J. Chem. Phys.* 125:014306
33. Parsons BF, Sheehan SM, Kautzman KE, Yen TA, Neumark DM. 2006. Photoelectron imaging of I_2^- at 5.826 eV. *J. Chem. Phys.* 125:244301
34. Calvi RMD, Andrews DH, Lineberger WC. 2007. Negative ion photoelectron spectroscopy of copper hydrides. *Chem. Phys. Lett.* 442:12–16
35. McCunn LR, Gardenier GH, Guasco TL, Elliott BM, Bopp JC, et al. 2008. Probing isomer interconversion in anionic water clusters using an Ar-mediated pump-probe approach: combining vibrational predissociation and velocity-map photoelectron imaging spectroscopies. *J. Chem. Phys.* 128:234311
36. Xing XP, Wang XB, Wang LS. 2008. Imaging intramolecular Coulomb repulsions in multiply charged anions. *Phys. Rev. Lett.* 101:083003
37. Sobhy MA, Castleman AW. 2007. Photoelectron imaging of copper and silver mono- and diamine anions. *J. Chem. Phys.* 126:154314
38. Cavanagh SJ, Gibson ST, Gale MN, Dedman CJ, Roberts EH, Lewis BR. 2007. High-resolution velocity-map-imaging photoelectron spectroscopy of the O^- photodetachment fine-structure transitions. *Phys. Rev. A* 76:052708
39. Ichino T, Andrews DH, Rathbone GJ, Misaizu F, Calvi RMD, et al. 2008. Ion chemistry of 1H-1,2,3-triazole. *J. Phys. Chem. B* 112:545–57
40. Elliott BM, McCunn LR, Johnson MA. 2008. Photoelectron imaging study of vibrationally mediated electron autodetachment in the type I isomer of the water hexamer anion. *Chem. Phys. Lett.* 467:32–36
41. Adams CL, Schneider H, Ervin KM, Weber JM. 2009. Low-energy photoelectron imaging spectroscopy of nitromethane anions: electron affinity, vibrational features, anisotropies, and the dipole-bound state. *J. Chem. Phys.* 130:074307
42. Gupta U, Reveles JU, Melko JJ, Khanna SN, Castleman AW. 2009. Electron delocalization in a non-cyclic all-metal III–V cluster. *Chem. Phys. Lett.* 480:189–92
43. Sobhy MA, Reveles JU, Gupta U, Khanna SN, Castleman AW. 2009. Photoelectron imaging and theoretical investigation of bimetallic $Bi_{1-2}Ga_{0-2}^-$ and Pb_{1-4}^- cluster anions. *J. Chem. Phys.* 130:054304
44. Goebbert DJ, Khuseynov D, Sanov A. 2009. Laboratory observation of the valence anion of cyanoacetylene, a possible precursor for negative ions in space. *J. Chem. Phys.* 131:161102
45. Mabbs R, Grumblin ER, Pichugin K, Sanov A. 2009. Photoelectron imaging: an experimental window into electronic structure. *Chem. Soc. Rev.* 38:2169–77

46. Velarde L, Habteyes T, Glass RS, Sanov A. 2009. Observation and characterization of the $\text{CH}_3\text{S}(\text{O})\text{CH}^-$ and $\text{CH}_3\text{S}(\text{O})\text{CH}^- \cdot \text{H}_2\text{O}$ carbene anions by photoelectron imaging and photofragment spectroscopy. *J. Phys. Chem. A* 113:3528–34
47. Van Duzor M, Wei J, Mbaiwa F, Mabbs R. 2009. The effect of intra-cluster photoelectron interactions on the angular distribution in $\text{I}^- \cdot \text{CH}_3\text{I}$ photodetachment. *J. Chem. Phys.* 131:204306
48. Goebbert DJ. 2012. Photoelectron imaging of CH^- . *Chem. Phys. Lett.* 551:19–25
49. Gessner O, Lee AMD, Shaffer JP, Reisler H, Levchenko SV, et al. 2006. Femtosecond multidimensional imaging of a molecular dissociation. *Science* 311:219–22
50. Grumbling ER, Mabbs R, Sanov A. 2011. Photoelectron imaging as a quantum chemistry visualization tool. *J. Chem. Educ.* 88:1515–20
51. Grumbling E, Sanov A. 2011. Photoelectron angular distributions in negative-ion photodetachment from mixed sp states. *J. Chem. Phys.* 135:164302
52. Sanov A, Grumbling ER, Goebbert DJ, Culberson LM. 2013. Photodetachment anisotropy for mixed s-p orbitals: 8/3 and other fractions. *J. Chem. Phys.* 138:054311
53. Culberson LM. 2013. *Molecular electronic structure via photoelectron imaging spectroscopy*. PhD Diss., Univ. Ariz., Tucson
54. Culberson LM, Blackstone CC, Sanov A. 2013. Photoelectron angular distributions of pyridinide: a benchmark application of the mixed s-p model to a truly polyatomic anion. *J. Phys. Chem. A* 117:11760–65
55. Culberson LM, Blackstone CC, Wysocki R, Sanov A. 2014. Selective deprotonation of oxazole and photoelectron imaging of the oxazolide anion. *Phys. Chem. Chem. Phys.* 16:527–32
56. Koopmans T. 1934. Über die Zuordnung von Wellenfunktionen und Eigenwerten zu den Einzelnen Elektronen Eines Atoms. *Physica* 1:104–13
57. Reed KJ, Zimmerman AH, Andersen HC, Brauman JI. 1976. Cross sections for photodetachment of electrons from negative ions near threshold. *J. Chem. Phys.* 64:1368–75
58. Landau LD, Lifshitz EM. 1977. *Quantum Mechanics: Nonrelativistic Theory*. Oxford: Pergamon
59. Cohen-Tannoudji C, Diu B, Laloë F. 1977. *Quantum Mechanics*. New York: Wiley
60. Wigner EP. 1948. On the behavior of cross sections near thresholds. *Phys. Rev.* 73:1002–9
61. Lineberger WC, Hotop H, Patterson TA. 1976. Photodetachment threshold processes. In *Electron and Photon Interactions with Atoms*, ed. H Kleinpoppen, MRC McDowell, pp. 125–32. New York: Plenum
62. Mead RD, Lykke KR, Lineberger WC. 1984. Photodetachment threshold laws. In *Electronic and Atomic Collisions*, ed. J Eichler, IV Hertel, N Stolterfoht, pp. 721–30. Amsterdam: Elsevier
63. Dill D, Dehmer JL. 1974. Electron-molecule scattering and molecular photoionization using multiple-scattering method. *J. Chem. Phys.* 61:692–99
64. Dill D. 1976. Fixed-molecule photoelectron angular distributions. *J. Chem. Phys.* 65:1130–33
65. Dixit SN, McKoy V. 1985. Theory of resonantly enhanced multiphoton processes in molecules. *J. Chem. Phys.* 82:3546–53
66. Dehmer JL, Dill D. 1978. Photo-ion angular distributions in dissociative photo-ionization of H_2 at 304 Å. *Phys. Rev. A* 18:164–71
67. Cooper J, Zare RN. 1968. Angular distributions in atomic anion photodetachment. *J. Chem. Phys.* 48:942–43
68. Park H, Zare RN. 1996. Molecular-orbital decomposition of the ionization continuum for a diatomic molecule by angle- and energy-resolved photoelectron spectroscopy 1. Formalism. *J. Chem. Phys.* 104:4554–67
69. Lin P, Lucchese RR. 2001. Studies of angular distributions and cross sections for photodetachment from the oxygen molecular anion. *J. Chem. Phys.* 114:9350–60
70. Dribinski V, Ossadtchi A, Mandelshtam VA, Reisler H. 2002. Reconstruction of Abel-transformable images: the Gaussian basis-set expansion Abel transform method. *Rev. Sci. Instrum.* 73:2634–42
71. Grumbling E, Sanov A. 2011. Partial-wave balance and charge-transfer-to-solvent in $\text{H}^-(\text{NH}_3)_n$ and $\text{NH}_2^-(\text{NH}_3)_n$ ($n = 0-5$) via anion photoelectron imaging. *J. Chem. Phys.* 135:164301
72. Wang LS, Xing XP, Wang XB. 2009. Photoelectron imaging of multiply charged anions: effects of intramolecular Coulomb repulsion and photoelectron kinetic energies on photoelectron angular distributions. *J. Chem. Phys.* 130:074301

73. Akin FA, Schirra LK, Sanov A. 2006. Photoelectron imaging study of the effect of monohydration on O_2^- photodetachment. *J. Phys. Chem. A* 110:8031–36
74. Velarde L, Habteyes T, Grumbling ER, Pichugin K, Sanov A. 2007. Solvent resonance effect on the anisotropy of $NO^-(N_2O)_n$ cluster anion photodetachment. *J. Chem. Phys.* 127:084302
75. Goebbert DJ, Pichugin K, Sanov A. 2009. Low-lying electronic states of CH_3NO_2 via photoelectron imaging of the nitromethane anion. *J. Chem. Phys.* 131:164308
76. Cooper J, Zare RN. 1968. Erratum: angular distributions in atomic anion photodetachment. *J. Chem. Phys.* 49:4252
77. Bethe HA, Salpeter EE. 1957. *Quantum Mechanics of One- and Two-Electron Atoms*. Berlin: Springer-Verlag. 368 pp.
78. Hanstorp D, Bengtsson C, Larson DJ. 1989. Angular distributions in photodetachment from O^- . *Phys. Rev. A* 40:670–75
79. Smith JR, Kim JB, Lineberger WC. 1997. High-resolution threshold photodetachment spectroscopy of OH^- . *Phys. Rev. A* 55:2036–43
80. Kim JB, Wenthold PG, Lineberger WC. 1998. Photoelectron spectroscopy of $OH^-(N_2O)_{n=1-5}$. *J. Chem. Phys.* 108:830–37
81. Brandon WD, Lee DH, Hanstorp D, Pegg DJ. 1998. Photodetachment of the C^- ion. *J. Phys. B* 31:751–60
82. Mabbs R, Surber E, Sanov A. 2005. Photoelectron anisotropy and channel branching ratios in the detachment of solvated iodide cluster anions. *J. Chem. Phys.* 122:054308
83. Aravind G, Gupta AK, Krishnamurthy M, Krishnakumar E. 2007. Spectral dependence of the asymmetry parameter in the photodetachment from As^- . *Phys. Rev. A* 75:042714
84. Aravind G, Ram NB, Gupta AK, Krishnakumar E. 2009. Probing the influence of channel coupling on the photoelectron angular distribution for the photodetachment from Cu^- . *Phys. Rev. A* 79:043411
85. Mbaiwa F, Wei J, Van Duzor M, Mabbs R. 2010. Threshold effects in $I^- \cdot CH_3CN$ and $I^- \cdot H_2O$ cluster anion detachment: the angular distribution as an indicator of electronic autodetachment. *J. Chem. Phys.* 132:134304
86. Mabbs R, Mbaiwa F, Wei J, Van Duzor M, Gibson ST, et al. 2010. Observation of vibration-dependent electron anisotropy in O_2^- photodetachment. *Phys. Rev. A* 82:011401
87. Van Duzor M, Mbaiwa F, Wei J, Singh T, Mabbs R, et al. 2010. Vibronic coupling in the superoxide anion: the vibrational dependence of the photoelectron angular distribution. *J. Chem. Phys.* 133:174311
88. Sobhy MA, Casalenuovo K, Reveles JU, Gupta U, Khanna SN, Castleman AW. 2010. Photoelectron imaging and density-functional investigation of bismuth and lead anions solvated in ammonia clusters. *J. Phys. Chem. A* 114:11353–63
89. Grumbling ER, Pichugin K, Velarde L, Sanov A. 2010. Further evidence for resonant photoelectron-solvent scattering in nitrous oxide cluster anions. *J. Phys. Chem. A* 114:1367–73
90. Reichle R, Helm H, Kiyani IY. 2003. Detailed comparison of theory and experiment of strong-field photodetachment of the negative hydrogen ion. *Phys. Rev. A* 68:063404
91. Hall JL, Siegel MW. 1968. Angular dependence of laser photodetachment of negative ions of carbon, oxygen, and hydrogen. *J. Chem. Phys.* 48:943–45
92. Breyer F, Frey P, Hotop H. 1978. High-resolution photoelectron spectrometry of negative-ions: fine-structure transitions in O^- and S^- photodetachment. *Z. Phys. A* 286:133–38
93. Slater JC. 1930. Atomic shielding constants. *Phys. Rev.* 36:57–64
94. Clementi E, Raimondi DL. 1963. Atomic screening constants from SCF functions. *J. Chem. Phys.* 38:2686–89
95. Scheer M, Bilodeau RC, Brodie CA, Haugen HK. 1998. Systematic study of the stable states of C^- , Si^- , Ge^- , and Sn^- via infrared laser spectroscopy. *Phys. Rev. A* 58:2844–56
96. Pegg DJ, Tang CY, Dellwo J, Alton GD. 1993. Angular distribution of electrons photodetached from the excited negative ion of carbon. *J. Phys. B* 26:L789–92
97. Buckingham AD, Orr BJ, Sichel JM. 1970. Angular distribution and intensity in molecular photoelectron spectroscopy I. General theory for diatomic molecules. *Philos. Trans. R. Soc. A* 268:147–57
98. Grumbling ER. 2010. *Electronic structure, intermolecular interactions and electron emission dynamics via anion photoelectron imaging*. PhD Diss., Univ. Ariz., Tucson. 257 pp.

99. Ortiz JV. 2004. Brueckner orbitals, Dyson orbitals, and correlation potentials. *Int. J. Quantum Chem.* 100:1131–35
100. Schafman BS, Wenthold PG. 2007. Regioselectivity of pyridine deprotonation in the gas phase. *J. Org. Chem.* 72:1645–51
101. Wren S, Vogelhuber KM, Garver JM, Kato S, Sheps L, et al. 2012. C-H bond strengths and acidities in aromatic systems: effects of nitrogen incorporation in mono-, di-, and triazines. *J. Am. Chem. Soc.* 134:6584–95
102. Shao Y, Molnar LF, Jung Y, Kussmann J, Ochsenfeld C, et al. 2006. Advances in methods and algorithms in a modern quantum chemistry program package. *Phys. Chem. Chem. Phys.* 8:3172–91
103. Krylov AI. 2008. Equation-of-motion coupled-cluster methods for open-shell and electronically excited species: the hitchhiker's guide to Fock space. *Annu. Rev. Phys. Chem.* 59:433–62
104. Culberson LM. 2013. *Molecular electronic structure via photoelectron imaging spectroscopy*. PhD Diss., Univ. Ariz., Tucson
105. Reichle R, Helm H, Kiyan IY. 2001. Photodetachment of H^- in a strong infrared laser field. *Phys. Rev. Lett.* 87:243001